JOURNAL OF SYNCHROTRON RADIATION

ISSN 1600-5775

Received 15 October 2018
Accepted 29 March 2019

Edited by M. Yabashi, RIKEN SPring-8 Center, Japan

[1] This article will form part of a virtual special issue on X-ray free-electron lasers.

Keywords: pulsed lasers; X-ray absorption spectroscopy; resonant inelastic X-ray scattering; soft X-rays; photon in/photon out instruments.

Scientific instruments for soft X-ray photon-in/photon-out spectroscopy on the PAL-XFEL[1]

Sang Han Park,[a] Jungbum Yoon,[b] Changsoo Kim,[b] Chanyong Hwang,[b] Dong-Hyun Kim,[c] Sang-Hyuk Lee[d] and Soonnam Kwon[a]*

[a]PAL-XFEL, Pohang Accelerator Laboratory, 77 Cheongam-Ro, Nam-Gu, Pohang, Gyeongbuk 37673, Republic of Korea, [b]Spin Convergence Research Team, Korea Research Institute of Standards and Science (KRISS), Daejeon 34113, Republic of Korea, [c]Department of Physics, Chungbuk National University, Cheongju, Chungbuk 28644, Republic of Korea, and [d]Advanced Instrumentation Institute, Korea Research Institute of Standards and Science (KRISS), Daejeon 34113, Republic of Korea. *Correspondence e-mail: snkwon@postech.ac.kr

An overview is given of the soft X-ray photon-in/photon-out instruments on the free-electron laser (FEL) beamline at the Pohang Accelerator Laboratory, and selected commissioning results are presented. The FEL beamline provides a photon energy of 270 to 1200 eV, with an energy bandwidth of 0.44%, an energy of 200 µJ per pulse and a pulse width of <50 fs (full width at half-maximum). The estimated total time resolution between optical laser and X-ray pulses is <100 fs. Instruments for X-ray absorption spectroscopy (XAS) and resonant inelastic X-ray scattering (RIXS) have been set up. X-ray magnetic circular dichroism spectra for a Co/Pt multilayer film and RIXS spectra for α-Fe_2O_3(100) have been obtained and the performance of the spectrometer has been evaluated.

1. Introduction

Ultra-fast pulsed lasers have been used to increase our understanding of the dynamics of materials (Dantus *et al.*, 1990; Chergui, 2014). However, these devices cannot provide element-specific information, and numerous efforts have been devoted to circumventing this limitation. Higher-harmonic-generated (HHG) lasers have achieved great success because the pulses can simultaneously provide both a high energy up to 100 eV and a pulse width as short as attoseconds (Sansone *et al.*, 2011; Kraus *et al.*, 2018). However, they still cannot provide full access to all atomic core levels.

The use of X-ray free-electron lasers (XFELs) as probes can continue to expand our understanding of the dynamics of materials by providing element-specific information about the evolution of the system and full access to almost all atomic core levels (Ackermann *et al.*, 2007; Allaria *et al.*, 2012; Emma *et al.*, 2010; Ishikawa *et al.*, 2012; Altarelli, 2011; Kang *et al.*, 2017). XFELs provide high-energy photons that can distinguish a material's atoms and ions by exciting their core electrons, typically with energy ranges from several tens of electron volts to 100 keV. The soft X-ray energy range is well matched to the *K* edges of elements from B to Ne, to the *L* edges of elements from S to Ge, and to the *M* edge of elements from Se to Gd. The soft X-rays generated on the PAL-XFEL facility can provide photons with an energy range from 270 to 1200 eV, a pulse energy of 200 µJ per pulse, a pulse width of <50 fs full width at half-maximum (FWHM) and an energy bandwidth of 0.44% (Park *et al.*, 2018). The XFEL can also provide a pump–probe capability. An external pump excites electrons in the material, then after a delay time an X-ray

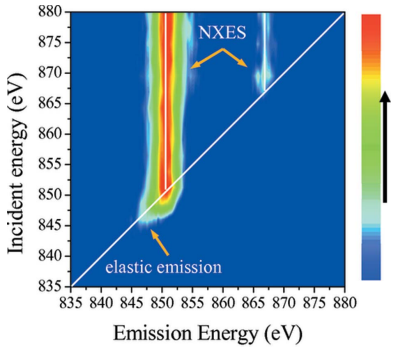

pulse probes the properties of the material as it relaxes. Two categories of pump–probe experiment can be used: 'photon-in/electron-out' and 'photon-in/photon-out'. In photon-in/electron-out experiments, the high peak fluence of the XFEL induces a space charge effect, which is a severe disturbance of the electron distribution in the sample, so the measurements are distorted (Hellmann *et al.*, 2009). To avoid this effect, the photon number must be $<10^7$ per pulse and the repetition rate must be increased; these adjustments are not possible in our facility, because it has a maximum repetition rate of 60 Hz. Therefore, we only considered photon-in/photon-out experiments.

First, we considered X-ray absorption spectroscopy (XAS) to probe the unoccupied states of materials. This method can use either transmission mode or fluorescence-yield mode. In transmission mode, the X-rays penetrate samples that are composed of a thin film, gas or liquid, and then the intensity of the transmitted X-rays is recorded. Fluorescence-yield-mode XAS is used for samples that X-rays cannot penetrate; in this case, the X-rays excite the sample, and the resulting scattered X-rays are collected and recorded by an X-ray spectrometer.

Second, we prepared for resonant inelastic X-ray scattering (RIXS), in which information can be obtained by analysis of the energy that is lost by X-rays that scatter inelastically from the sample. These data are collected using an RIXS spectrometer (Park *et al.*, 2018). Energy-loss spectra, measured to a fraction of an electron volt, can probe subtle features of electronic structure, correlation and bonding.

After a rigorous commissioning process, we demonstrated the feasibility and estimated the performance of each experimental setup. We verified transmission-mode XAS by measuring the X-ray magnetic circular dichroism (XMCD) of a Co/Pt multilayer film. We verified fluorescence-yield-mode XAS using an RIXS spectrometer to measure the XAS spectra from metal single crystals. We also obtained typical RIXS spectra from single crystals of Ni(111) and α-Fe_2O_3(100). The optical pump and X-ray pulses were synchronized to match a temporal overlap of <100 fs.

2. Beamline and endstation

The beamline (Fig. 1, Table 1) consists mainly of a gas attenuator, offset mirrors, a monochromator system, focusing mirrors and an endstation. The gas attenuator reduces the photon flux by a factor of as much as ten. The major function of the offset mirrors is to isolate the other optical elements from hazardous radiation such as γ-rays and *bremsstrahlung* radiation that is generated in the undulators and the electron dump. The first mirror is planar, while the second one is concavely cylindrical with a radius of 3493.2 m, which yields a horizontal focal point 93.01 m downstream from the source point. This focal point is a source point for a horizontal focus mirror (M4) located at 111.01 m with a demagnification of 9 (18:2) at the sample position. In the vertical direction, the pre-mirror of the monochromator focuses the beam on the exit slit of the monochromator at 89.01 m. This point is a source point of a vertical refocus mirror (M5) that has a vertical demagnification of 15 (22.5:1.5). The spot size of the monochromatic XFEL is controlled vertically by the vertical exit slit and is fixed horizontally at <50 µm (Park *et al.*, 2018).

The full energy range of 270–1200 eV is covered by two VLS gratings: G1 covers 270–600 eV with a grating frequency G = 100 lines mm^{-1}, and G2 covers 600–1200 eV with G = 200 lines mm^{-1}. The incident angle of the photon beam onto the grating is designed to be 88.26–88.68°. The final diffracted beam is set to be horizontal, from which the diffracted angles from the normal of the grating surface are designed to be 88.74–88.34°. The focal point is 20 m from the VLS grating.

The endstation is installed downstream of a Kirkpatrick–Baez (K–B) mirror system. The laser-in coupling is located between the interaction chamber and the K–B mirror system to make the pump laser beam and XFEL beam collinear. Two photon-flux monitors are installed: one is a gas detector located downstream of the gas attenuator, and one is a Pt (5 nm)/Si_3N_4 (200 nm) film combined with a centre-holed micro-channel plate (MCP) and located downstream of the exit slit. The former is used for an unmonochromatized XFEL

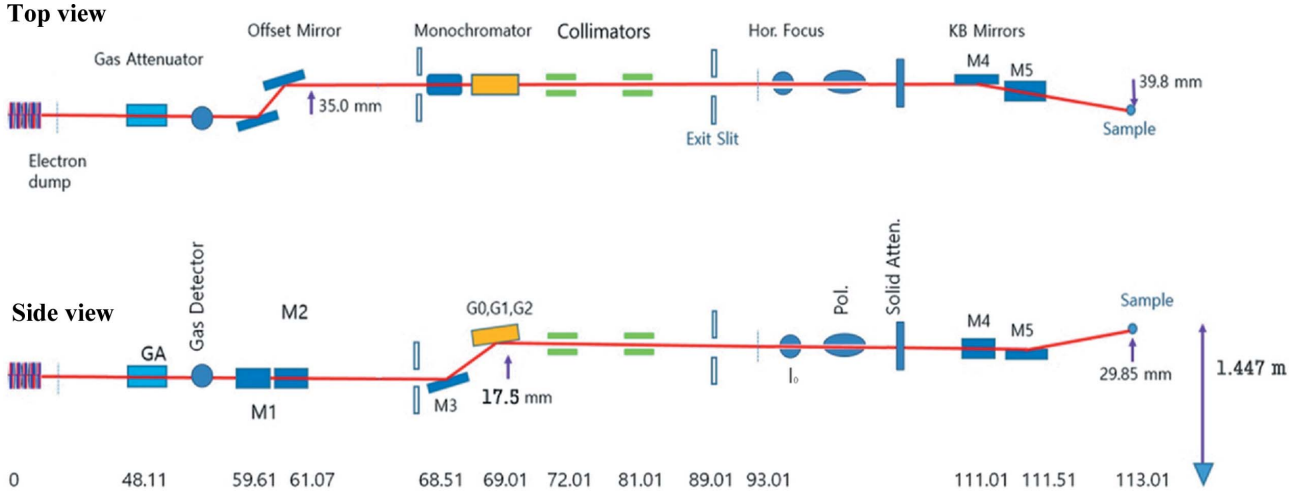

Figure 1
Schematic diagrams of the SSS beamline optics and main components (as defined in Table 1).

Table 1
Main components of the soft X-ray beamline.

Optical element	Description	Coating/ substrate	Dimensions (l × w × t) (mm)	Radius (m)	Incidence angle [mrad (°)]	Distance from source (m)
GA/GMD						35.0/40.0
M1	Plane mirror, first offset mirror	B_4C/Si	600 × 50 × 50	∞	12 (0.688)	59.61
M2	Cylindrical mirror, second offset mirror	B_4C/Si	600 × 50 × 50	3493.2	12 (0.688)	61.068
Entrance aperture	Four-jaw slit system	B_4C/Si				68.0
M3	Cylindrical mirror, pre-mirror for grating	B_4C/Si	300 × 60 × 60	1808.21	17.44 (1.0)	68.51
G0, G1, G2	Plane mirror/plane varied line spacing gratings	B_4C/Si	170 × 50 × 40	∞	17.44 (1.0)	69.01
C1	Collimator 1	Tungsten	ID 20, OD 50, *l* 100			72.01
C2	Collimator 2	Tungsten	ID 20, OD 50, *l* 100			81.01
Vert. slit	Vertical slit	B_4C	5 × 0.030			89.01
Hor. foc.	Horizontal focus					93.01
I_0	Centre-holed MCP	MCP+Pt/SiN				100.0
Pol.	Circular polarizer	Co/Fe/Ni films/ SiN				105.0
SA	Solid attenuator	Au/SiN				106.0
M4	Elliptical mirror, horizontal refocusing mirror	B_4C/Si	400 × 50 × 50	360.1	10 (0.573)	111.01
M5	Elliptical mirror, vertical refocusing mirror	B_4C/Si	400 × 50 × 50	281.26	10 (0.573)	111.51
LIN	Laser-in coupling chamber	Centre-hole mirror, Au/Glass	Circular (50.08 diameter)			
Sample						113.01

beam, whereas the latter is used for a monochromatized XFEL beam, and is also used as a reference signal I_0 for XAS measurements. Downstream of the I_0 monitor, a circular polarizer and solid attenuators are installed in sequence.

3. Commissioning results

All optics in the soft X-ray beamline are coated with B_4C to maximize throughput and endure X-ray damage, but X-ray absorption by the mirror surfaces is unavoidable. To allow correction, the absorption of B_4C should be quantified without a sample before experiments. Thus, the XAS of B_4C at the C *K* edge was obtained for the beamline mirrors [Fig. 2(*a*)]. The spectrum showed the most significant absorption peak at 285 eV, but also had absorption features at higher energies than this. We used the full bandwidth of the XFEL, so the spectrum shows broad features. The main absorption peak is a convolution of peaks at 284.5, 287 and 288 eV and is related to the sp^2 bonding of B_4C; the peak at higher energy is related to sp^3 bonding (Jiménez *et al.*, 1998). The intensity of the XFEL reflected by the mirrors was measured by averaging the observed fluorescence of the XFEL on a Ce:YAG crystal at the sample position using a CCD camera (Allied Vision, Manta G-046). Then the absorbance *A* of C 1*s* was calculated from the difference Δ in the intensities *I* from the pre-edge region as $A = \log[I/(I - \Delta)]$. The degradation of the mirrors can be monitored by tracing the change in the peak intensity of the C 1*s* XAS spectrum.

For measurements of fluorescence-yield-mode XAS, fluorescent photons from the sample were collected by an RIXS spectrometer in which the mirror and grating are aligned parallel using undispersed zero-order; the angle between the incident and outgoing X-rays is set to 90°. We measured the fluorescence-yield-mode XAS spectrum of the Cr *L* edges [Fig. 2(*b*)]. The Cr L_2 edge has a larger fluorescence intensity than the Cr L_3 edge. This difference occurs because the effectiveness of self-absorption and saturation effects increases as the photon energy decreases in the soft X-ray region (Eisebitt *et al.*, 1993; Asakura *et al.*, 2016). The fluor-

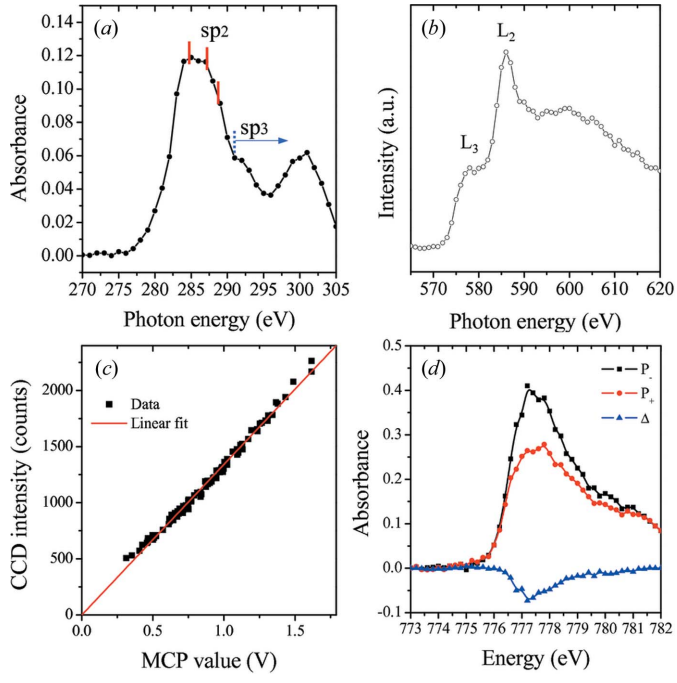

Figure 2
(*a*) The XAS spectrum of the C *K* edge for B_4C-coated mirrors on the SSS beamline. (*b*) Fluorescence-yield mode XAS spectra of the Cr *L* edges. (*c*) The correlation between MCP I_0 and transmitted X-rays measured using the PI-MTE CCD. (*d*) Transmission-mode XAS spectra and XMCD data for the Co L_3 edge of a Co/Pt multilayer with a circular polarizer. We used the full bandwidth of the XFEL to obtain panels (*a*) and (*b*), and a monochromated XFEL for panels (*c*) and (*d*).

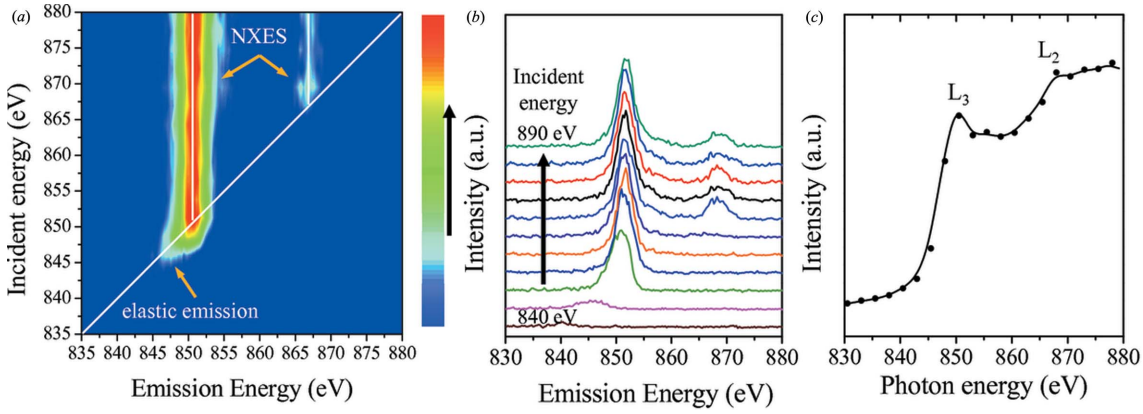

Figure 3
RIXS data for a single Ni(111) crystal measured at the Ni *L* edge. (*a*) The RIXS map and (*b*) the RIXS spectra of Ni as a function of the incident photon energies. (*c*) The PFY-mode XAS spectrum for Ni by integrating the RIXS spectra for each incident photon energy.

escence intensity at each energy was measured using a CCD detector (Andor, Newton DO940P-BN).

In the transmission-mode XAS setup, the XFEL beam passes sequentially through the circular polarizer, the I_0 monitor, the solid attenuator, the sample and the detector. The intensity of the transmitted XFEL beam was measured using an in-vacuum CCD detector (Princeton Instruments, PI-MTE:2048B) with a parylene (100 nm)/aluminium (100 nm) filter to exclude the optical laser. The pulse-by-pulse intensity was recorded using an external trigger synchronized to the XFEL. With vertical binning mode acquisition, the PI-MTE CCD can collect data for all pulses at 10 Hz. However, due to inevitable pulse-to-pulse intensity variation of the XFEL beam, the intensity of I_0 should be measured for each pulse, especially for monochromatic X-rays. To measure the intensity of the incident X-rays for each pulse we used a centre-holed MCP in combination with a Pt-coated SiN membrane. When the XFEL beam passes through the Pt-coated membrane, photoelectrons that are emitted by the Pt surface are collected by the MCP. The I_0 MCP and CCD values for each pulse are recorded over time on a microsecond scale. For normalization, the CCD value is divided by the I_0 MCP value that is recorded at the same time. A linear regression of I_0 MCP on the CCD had a coefficient of determination $r^2 = 0.99$ [Fig. 2(*c*)].

To generate circularly polarized X-rays, we used a ferromagnetic film polarizer. When a linearly polarized X-ray beam passes through a ferromagnetic film, part of the X-ray beam becomes circularly polarized; the proportion depends on the angle between the X-ray beam and the magnetic field (Pfau *et al.*, 2010). We used a permanent magnet to apply a magnetic field of 0.1 T in the in-plane direction to a Co film. The incident angle of the XFEL beam to the normal direction of the Co film is adjustable and set to 45° for the measurement [Fig. 1(*c*)]. The sign of the polarization can be changed by rotating the whole polarizer arrangement by 180°. Using a circularly polarized XFEL beam, transmission-mode XAS was measured at the Co L_3 edge of a Co (0.5 nm)/Pt (0.8 nm) multilayer that had a total thickness of 80 nm [Fig. 2(*d*)] to achieve large absorption intensity. The 0.1 T magnetic field was applied to the sample in the out-of-plane direction, which is parallel to the XFEL beam. The Co L_3 edge at 776 eV shows a different absorbance as the sign of the circularly polarized light changes (Nolting *et al.*, 2000). The difference in the absorption intensities of opposite polarizations is due to the spin alignment of the Co/Pt multilayer sample. Therefore, the magnetic dichroism effect [Fig. 2(*d*)] shows that the Co/Pt multilayer has bulk ferromagnetism with out-of-plane magnetization. The degree of circular polarization was highest (0.17) at 778.2 eV (Kortright *et al.*, 1997).

An RIXS map for a single Ni(111) crystal was obtained. The incidence angle to the surface normal of the incoming X-rays was 50° and the emitted photons were detected in the horizontal plane in the direction perpendicular to the direction of the incident X-ray beam. The RIXS map [Fig. 3(*a*)] and the RIXS spectra [Fig. 3(*b*)] both show elastic and non-resonant X-ray emission. The elastic emission showed zero energy loss on the map near resonance, whereas the non-resonant X-ray emission peak showed an energy loss (the energy difference between the incident and emitted photons) that increased as the incident photon energy increased. When the incident photon energy was just less than the Ni L_3 edge (851 eV), only a small elastic peak was observed. For our experimental geometry, in which the angle between the XFEL beam and the RIXS spectrometer is 90°, elastic emission is forbidden. However, a small elastic emission can be observed because of the roughness of the sample surface and imperfect geometry (Ament *et al.*, 2011). When the photon energy of the incident XFEL beam is greater than the binding energy of Ni $2p_{3/2}$, the emitted photon energy is constant because the main emission process involves recombination of the Fermi-level electrons (Ni 3*d*) with holes at Ni $2p_{3/2}$ to emit photons. As the incident photon energy was increased to 876 eV, the emission related to Ni $2p_{1/2}$ started to appear, with a small intensity. Fluorescence-yield-mode XAS could be obtained by integrating the intensity of the emission spectra for the Ni *L* edge in the energy range from 830 to 880 eV.

Fluorescence-yield-mode XAS was measured for a single α-Fe_2O_3(100) crystal at the Fe L_3 edge [Fig. 4(*a*)]. The XAS spectrum shows a t_{2g} peak at 707.5 eV and an e_g peak at 709.5 eV due to the octahedral ligand field splitting (Abbate *et al.*, 1992). Then RIXS spectra were measured at incident energies of 707.5 eV (= t_{2g}) [Figs. 4(*b*)] and 709.5 eV (= e_g)

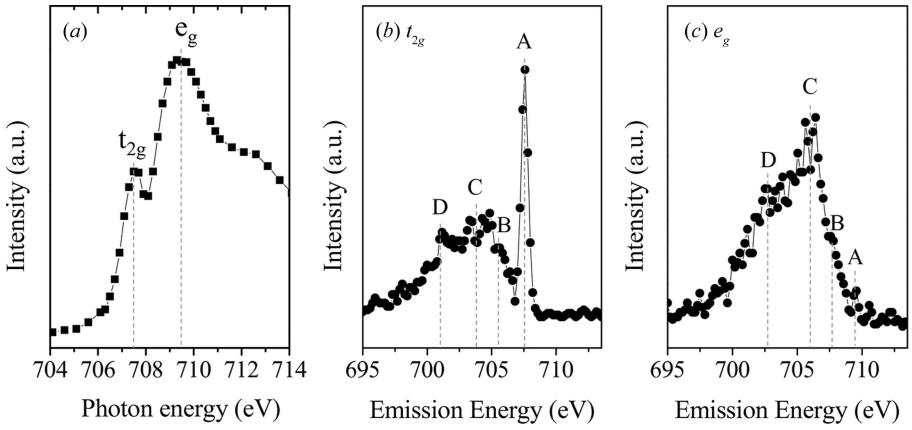

Figure 4
(*a*) The XAS spectrum of a single α-Fe_2O_3 crystal at the Fe L_3 edge. (*b*) and (*c*) RIXS spectra at the absorption edge of (*b*) t_{2g} (707.5 eV) and (*c*) e_g (709.5 eV). The points marked A–D indicate: A elastic emission, and B, C, D inelastic emission.

[Fig. 4(*c*)]. Elastic emissions had the highest emission energy in both spectra [point A in Figs. 4(*b*) and 4(*c*)]; this elastic peak had FWHM = 0.6 eV. We used these elastic peaks to calibrate the measured energy of the outgoing photon. The fundamental energy resolution of our spectrometer at the Fe *L* edge is about 0.6 eV, which explains the lower resolution of our spectra compared with a previous report on RIXS of Fe_2O_3 (Miyawaki *et al.*, 2017).

The inelastic emission features [Fig. 4(*c*), points B–D] appear at 2 eV (B), 4 eV (C) and 6.5 eV (D) lower than the elastic peak (A). The features with 2 eV energy loss correspond to the band-gap excitation in which the bulk band gap of α-Fe_2O_3 is 2.0 eV (Duda *et al.*, 2000). The other energy-loss features (C and D) are related to the charge-transfer excitation from unoccupied O 2*p* to unoccupied Fe 3*d* (Vayssieres *et al.*, 2005). The intensity of the elastic emission peak is higher and the intensity of the charge-transfer emission peaks are both lower in the emission spectrum at t_{2g} than at e_g. These results indicate that the t_{2g} state is more localized than the e_g state, so in the e_g state charge transfer occurs preferentially over elastic emission.

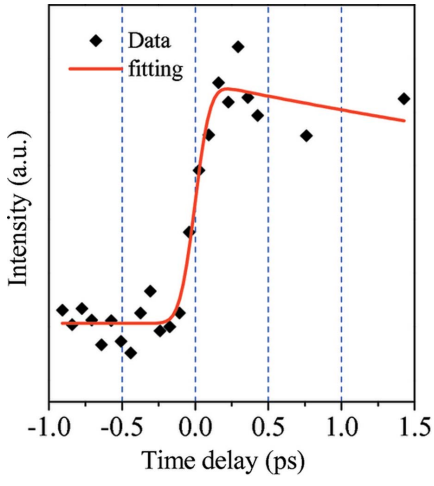

Figure 5
Transmission curves of the 400 nm laser beam as a function of time delay between the X-ray pump and laser probe on a Ce:YAG crystal. The temporal overlap between the optical laser and the XFEL is matched within about 100 fs in FWHM.

Optical-pump XFEL-probing is one of most important experimental techniques to use an XFEL beam. An XFEL beam with an ultra-short pulse width allows investigation of dynamics in the femtosecond range. For this experiment, synchronization between the X-ray beam and the pump laser must also be in the femtosecond range. At first, a fast photodiode (Hamamatsu, G4176) connected to an oscilloscope (Tektronix, DPO71254C) was used to achieve synchronization within ∼50 ps between the optical laser and the XFEL. To increase the precision of the match of temporal overlap, we used a reference Ce:YAG crystal. By measuring the intensity (Fig. 5) of an optical laser through the transparent Ce:YAG crystal in the visible range, we conducted an XFEL-pump optical-laser-probe experiment that requires a delay time of ∼1 ps. The intensity of the transmitted optical laser beam is measured using a photodiode (Hamamatsu, S3590-09). The intensity is integrated by a gate integrator (Stanford Research Systems, SR250) for every pulse, and 300 pulses are averaged for each data point without normalization. The rising edge of the transmission change (Fig. 5) represents the temporal overlap between the optical laser and XFEL beams. When the curve is fitted with a modulated Gaussian function, the width of the slope is <100 fs FWHM, which is much shorter than in our previous report (Park *et al.*, 2018). The decrease occurs because we have changed the measurement geometry from reflection to transmission. Then we obtained an enhanced time resolution, and we suggest that this improvement is a result of the removal of possible diffuse reflection, which occurs when the optical laser is reflected from the YAG crystal. Part of the reflection comes from one surface of the Ce:YAG crystal, and part comes from the opposite surface. When time zero is measured in transmission mode, this influence of diffuse reflection should be much reduced.

4. Conclusions

Instruments for photon-in/photon-out spectroscopy have been installed and tested on the soft X-ray FEL beamline PAL-XFEL. Major results such as XMCD of a Co/Pt multilayer film, fluorescence-yield-mode XAS of various transition metals at their *L* edges, and RIXS spectra of single crystals of Ni(111) and α-Fe_2O_3(100) have been presented. This beamline provides intense (2×10^{12} photons per pulse) beams with a short total time resolution (<100 fs).

Funding information

This work was supported by the Ministry of Science and ICT of Korea, and by a Basic Science Research Programme funded

by the Ministry of Education (grant No. NRF-2017-R1D1A1A02018484). The authors also acknowledge the use of the SSS beamline at PAL-XFEL (grant No. 2017-2nd-SSS-009).

References

Abbate, M., de Groot, F. M. F., Fuggle, J. C., Fujimori, A., Strebel, O., Lopez, F., Domke, M., Kaindl, G., Sawatzky, G. A., Takano, M., Takeda, Y., Eisaki, H. & Uchida, S. (1992). *Phys. Rev. B*, **46**, 4511–4519.

Ackermann, W., Asova, G., Ayvazyan, V., Azima, A., Baboi, N., Bähr, J., Balandin, V., Beutner, B., Brandt, A., Bolzmann, A., Brinkmann, R., Brovko, O. I., Castellano, M., Castro, P., Catani, L., Chiadroni, E., Choroba, S., Cianchi, A., Costello, J. T., Cubaynes, D., Dardis, J., Decking, W., Delsim-Hashemi, H., Delserieys, A., Di Pirro, G., Dohlus, M., Düsterer, S., Eckhardt, A., Edwards, H. T., Faatz, B., Feldhaus, J., Flöttmann, K., Frisch, J., Fröhlich, L., Garvey, T., Gensch, U., Gerth, Ch., Görler, M., Golubeva, N., Grabosch, H. -J., Grecki, M., Grimm, O., Hacker, K., Hahn, U., Han, J. H., Honkavaara, K., Hott, T., Hüning, M., Ivanisenko, Y., Jaeschke, E., Jalmuzna, W., Jezynski, T., Kammering, R., Katalev, V., Kavanagh, K., Kennedy, E. T., Khodyachykh, S., Klose, K., Kocharyan, V., Körfer, M., Kollewe, M., Koprek, W., Korepanov, S., Kostin, D., Krassilnikov, M., Kube, G., Kuhlmann, M., Lewis, C. L. S., Lilje, L., Limberg, T., Lipka, D., Löhl, F., Luna, H., Luong, M., Martins, M., Meyer, M., Michelato, P., Miltchev, V., Möller, W. D., Monaco, L., Müller, W. F. O., Napieralski, O., Napoly, O., Nicolosi, P., Nölle, D., Nuñez, T., Oppelt, A., Pagani, C., Paparella, R., Pchalek, N., Pedregosa-Gutierrez, J., Petersen, B., Petrosyan, B., Petrosyan, G., Petrosyan, L., Pflüger, J., Plönjes, E., Poletto, L., Pozniak, K., Prat, E., Proch, D., Pucyk, P., Radcliffe, P., Redlin, H., Rehlich, K., Richter, M., Roehrs, M., Roensch, J., Romaniuk, R., Ross, M., Rossbach, J., Rybnikov, V., Sachwitz, M., Saldin, E. L., Sandner, W., Schlarb, H., Schmidt, B., Schmitz, M., Schmüser, P., Schneider, J. R., Schneidmiller, E. A., Schnepp, S., Schreiber, S., Seidel, M., Sertore, D., Shabunov, A. V., Simon, C., Simrock, S., Sombrowski, E., Sorokin, A. A., Spanknebel, P., Spesyvtsev, R., Staykov, L., Steffen, B., Stephan, F., Stulle, F., Thom, H., Tiedtke, K., Tischer, M., Toleikis, S., Treusch, R., Trines, D., Tsakov, I., Vogel, E., Weiland, T., Weise, H., Wellhöfer, M., Wendt, M., Will, I., Winter, A., Wittenburg, K., Wurth, W., Yeates, P., Yurkov, M. V., Zagorodnov, I. & Zapfe, K. (2007). *Nat. Photon.* **1**, 336–342.

Allaria, E., Appio, R., Badano, L., Barletta, W. A., Bassanese, S., Biedron, S. G., Borga, A., Busetto, E., Castronovo, D., Cinquegrana, P., Cleva, S., Cocco, D., Cornacchia, M., Craievich, P., Cudin, I., D'Auria, G., Dal Forno, M., Danailov, M. B., De Monte, R., De Ninno, G., Delgiusto, P., Demidovich, A., Di Mitri, S., Diviacco, B., Fabris, A., Fabris, R., Fawley, W., Ferianis, M., Ferrari, E., Ferry, S., Froehlich, L., Furlan, P., Gaio, G., Gelmetti, F., Giannessi, L., Giannini, M., Gobessi, R., Ivanov, R., Karantzoulis, E., Lonza, M., Lutman, A., Mahieu, B., Milloch, M., Milton, S. V., Musardo, M., Nikolov, I., Noe, S., Parmigiani, F., Penco, G., Petronio, M., Pivetta, L., Predonzani, M., Rossi, F., Rumiz, L., Salom, A., Scafuri, C., Serpico, C., Sigalotti, P., Spampinati, S., Spezzani, C., Svandrlik, M., Svetina, C., Tazzari, S., Trovo, M., Umer, R., Vascotto, A., Veronese, M., Visintini, R., Zaccaria, M., Zangrando, D. & Zangrando, M. (2012). *Nat. Photon.* **6**, 699–704.

Altarelli, M. (2011). *Nucl. Instrum. Methods Phys. Res. B*, **269**, 2845–2849.

Ament, L. J. P., van Veenendaal, M., Devereaux, T. P., Hill, J. P. & van den Brink, J. (2011). *Rev. Mod. Phys.* **83**, 705–767.

Asakura, D., Hosono, E., Nanba, Y., Zhou, H., Okabayashi, J., Ban, C., Glans, P.-A., Guo, J., Mizokawa, T., Chen, G., Achkar, A. J., Hawthron, D. G., Regier, T. Z. & Wadati, H. (2016). *AIP Adv.* **6**, 035105.

Chergui, M. (2014). *Faraday Discuss.* **171**, 11–40.

Dantus, M., Bowman, R. M. & Zewail, A. H. (1990). *Nature*, **343**, 737–739.

Duda, L.-C., Nordgren, J., Dräger, G., Bocharov, S. & Kirchner, Th. (2000). *J. Electron Spectrosc. Relat. Phenom.* **110–111**, 275–285.

Eisebitt, S., Böske, T., Rubensson, J. -E. & Eberhardt, W. (1993). *Phys. Rev. B*, **47**, 14103–14109.

Emma, P., Akre, R., Arthur, J., Bionta, R., Bostedt, C., Bozek, J., Brachmann, A., Bucksbaum, P., Coffee, R., Decker, F.-J., Ding, Y., Dowell, D., Edstrom, S., Fisher, A., Frisch, J., Gilevich, S., Hastings, J., Hays, G., Hering, Ph., Huang, Z., Iverson, R., Loos, H., Messerschmidt, M., Miahnahri, A., Moeller, S., Nuhn, H. -D., Pile, G., Ratner, D., Rzepiela, J., Schultz, D., Smith, T., Stefan, P., Tompkins, H., Turner, J., Welch, J., White, W., Wu, J., Yocky, G. & Galayda, J. (2010). *Nat. Photon.* **4**, 641–647.

Hellmann, S., Rossnagel, K., Marczynski-Bühlow, M. & Kipp, L. (2009). *Phys. Rev. B*, **79**, 035402.

Ishikawa, T., Aoyagi, H., Asaka, T., Asano, Y., Azumi, N., Bizen, T., Ego, H., Fukami, K., Fukui, T., Furukawa, Y., Goto, S., Hanaki, H., Hara, T., Hasegawa, T., Hatsui, T., Higashiya, A., Hirono, T., Hosoda, N., Ishii, M., Inagaki, T., Inubushi, Y., Itoga, T., Joti, Y., Kago, M., Kameshima, T., Kimura, H., Kirihara, Y., Kiyomichi, A., Kobayashi, T., Kondo, C., Kudo, T., Maesaka, H., Maréchal, X. M., Masuda, T., Matsubara, S., Matsumoto, T., Matsushita, T., Matsui, S., Nagasono, M., Nariyama, N., Ohashi, H., Ohata, T., Ohshima, T., Ono, S., Otake, Y., Saji, C., Sakurai, T., Sato, T., Sawada, K., Seike, T., Shirasawa, K., Sugimoto, T., Suzuki, S., Takahashi, S., Takebe, H., Takeshita, K., Tamasaku, K., Tanaka, H., Tanaka, R., Tanaka, T., Togashi, T., Togawa, K., Tokuhisa, A., Tomizawa, H., Tono, K., Wu, S., Yabashi, M., Yamaga, M., Yamashita, A., Yanagida, K., Zhang, C., Shintake, T., Kitamura, H. & Kumagai, N. (2012). *Nat. Photon.* **6**, 540–544.

Jiménez, I., Sutherland, D. G. J., van Buuren, T., Carlisle, J. A., Terminello, L. J. & Himpsel, F. J. (1998). *Phys. Rev. B*, **57**, 13167–13174.

Kang, H.-S., Min, C.-K., Heo, H., Kim, C., Yang, H., Kim, G., Nam, I., Baek, S. Y., Choi, H.-J., Mun, G., Park, B. R., Suh, Y. J., Shin, D. C., Hu, J., Hong, J., Jung, S., Kim, S.-H., Kim, K.-H., Na, D., Park, S. S., Park, Y. J., Han, J.-H., Jung, Y. G., Jeong, S. H., Lee, H. G., Lee, S., Lee, S., Lee, W.-W., Oh, B., Suh, H. S., Parc, Y. W., Park, S.-J., Kim, M. H., Jung, N.-S., Kim, Y.-C., Lee, M.-S., Lee, B.-H., Sung, C.-W., Mok, I.-S., Yang, J.-M., Lee, C.-S., Shin, H., Kim, J. H., Kim, Y., Lee, J. H., Park, S.-Y., Kim, J., Park, J., Eom, I., Rah, S., Kim, S., Nam, K. H., Park, J., Park, J., Kim, S., Kwon, S., Park, S. H., Kim, K. S., Hyun, H., Kim, S. N., Kim, S., Hwang, S.-M., Kim, M. J., Lim, C.-Y., Yu, C.-J., Kim, B.-S., Kang, T.-H., Kim, K.-W., Kim, S.-H., Lee, H.-S., Lee, H.-S., Park, K.-H., Koo, T.-Y., Kim, D.-E. & Ko, I. S. (2017). *Nat. Photon.* **11**, 708–713.

Kortright, J. B., Kim, S.-K., Warwick, T. & Smith, N. V. (1997). *Appl. Phys. Lett.* **71**, 1446–1448.

Kraus, P. M., Zürch, M., Cushing, S. K., Neumark, D. M. & Leone, S. R. (2018). *Nat. Rev. Chem.* **2**, 82–94.

Miyawaki, J., Suga, S., Fujiwara, H., Urasaki, M., Ikeno, H., Niwa, H., Kiuchi, H. & Harada, Y. (2017). *Phys. Rev. B*, **96**, 214420.

Nolting, F., Scholl, A., Stohr, J., Seo, J. W., Fompeyrine, J., Siegwart, H., Locquet, J. -P., Anders, S., Luning, J., Fullerton, E. E., Toney, M. F., Scheinfein, M. R. & Padmore, H. A. (2000). *Nature*, **405**, 767–769.

Park, S. H., Kim, M., Min, C.-K., Eom, I., Nam, I., Lee, H.-S., Kang, H.-S., Kim, H.-D., Jang, H. Y., Kim, S., Hwang, S. M., Park, G. S., Park, J., Koo, T. Y. & Kwon, S. (2018). *Rev. Sci. Instrum.* **89**, 055105.

Pfau, B., Günther, C. M., Könnecke, R., Guehrs, E., Hellwig, O., Schlotter, W. F. & Eisebitt, S. (2010). *Opt. Express*, **18**, 13608.

Sansone, G., Poletto, L. & Nisoli, M. (2011). *Nat. Photon.* **5**, 656–663.

Vayssieres, L., Sathe, C., Butorin, S. M., Shuh, D. K., Nordgren, J. & Guo, J. (2005). *Adv. Mater.* **17**, 2320–2323.